THE JOURNAL OF BIOLOGICAL CHEMISTRY VOL. 281, NO. 32, pp. 22865–22874, August 11, 2006

Iron Regulation and the Cell Cycle

IDENTIFICATION OF AN IRON-RESPONSIVE ELEMENT IN THE 3′-UNTRANSLATED REGION OF HUMAN CELL DIVISION CYCLE 14A mRNA BY A REFINED MICROARRAY-BASED SCREENING STRATEGY[*] [S]

Received for publication, April 24, 2006, and in revised form, May 24, 2006 Published, JBC Papers in Press, June 7, 2006, DOI 10.1074/jbc.M603876200

Mayka Sanchez[‡§], Bruno Galy[‡], Thomas Dandekar[¶], Peter Bengert[¶‖], Yevhen Vainshtein[‡], Jens Stolte[‡], Martina U. Muckenthaler[§1], and Matthias W. Hentze[‡2]

From the [‡]European Molecular Biology Laboratory, Meyerhofstrasse 1, 69117 Heidelberg, the [§]Department of Pediatric Oncology, Hematology and Immunology, University of Heidelberg, Im Neuenheimer Feld 153, 69120 Heidelberg, the [¶]Department of Bioinformatics, Biozentrum, University of Würzburg, Am Hubland, 97074 Würzburg, and the [‖]Biochemistry Centre, University of Heidelberg, Im Neuenheimer Feld 365, 69120 Heidelberg, Germany

Iron regulatory proteins (IRPs) 1 and 2 post-transcriptionally control mammalian iron homeostasis by binding to iron-responsive elements (IREs), conserved RNA stem-loop structures located in the 5′- or 3′-untranslated regions of genes involved in iron metabolism (*e.g. FTH1*, *FTL*, and *TFRC*). To identify novel IRE-containing mRNAs, we integrated biochemical, biocomputational, and microarray-based experimental approaches. IRP/IRE messenger ribonucleoproteins were immunoselected, and their mRNA composition was analyzed using an IronChip microarray enriched for genes predicted computationally to contain IRE-like motifs. Among different candidates, this report focuses on a novel IRE located in the 3′-untranslated region of the cell division cycle 14A mRNA. We show that this IRE motif efficiently binds both IRP1 and IRP2. Differential splicing of cell division cycle 14A produces IRE- and non-IRE-containing mRNA isoforms. Interestingly, only the expression of the IRE-containing mRNA isoforms is selectively increased by cellular iron deficiency. This work describes a new experimental strategy to explore the IRE/IRP regulatory network and uncovers a previously unrecognized regulatory link between iron metabolism and the cell cycle.

Iron is an essential nutrient that can cause cell damage when present in excess. Systems that control cellular and systemic iron homeostasis have evolved to ensure adequate iron supply while preventing overload. The iron regulatory proteins (IRPs)[3] 1 and 2 play a central role in cellular iron metabolism by coordinately regulating the post-transcriptional expression of genes containing iron-responsive elements (IREs) in their 5′- or 3′-untranslated regions (UTRs). IRE-containing mRNAs encode proteins of iron acquisition (transferrin receptor 1 (*TFRC*) and divalent metal transporter 1 (*SLC11A2*-DMT1-DCT1-NRAMP2)), storage (*FTH1*, or ferritin heavy polypeptide 1; *FTL*, or ferritin light polypeptide), utilization (erythroid 5′-aminolevulinic acid synthase (*ALAS2* or eALAS), mitochondrial aconitase, *Drosophila* succinate dehydrogenase (*SDH*)), and export (*SLC40A1*-FPN1-IREG1-MTP1) (1). Independently, both IRPs inhibit translation initiation when bound to 5′-UTR IREs (*e.g. FTH1* and *FTL* mRNAs), whereas their association with the 3′-UTR IREs of the *TFRC* mRNA decreases its turnover (2–4). Although IRP1-deficient mice present no steady-state phenotypic abnormalities (5, 6), $Irp2^{-/-}$ animals display microcytosis associated with abnormal body iron distribution (5, 7) and have been reported to suffer from an overt, late onset, neurodegenerative disease (8). Early embryonic lethality in mice lacking both proteins indicates that the IRP/IRE regulatory network is essential (9). In humans, failure to coordinate the expression of IRE-containing genes is associated with pathological conditions, as illustrated by the autosomal dominant hyperferritinemia-cataract syndrome observed in patients carrying mutations in the *FTL* IRE (10), or by an autosomally dominant iron overload syndrome associated with a mutation in the *FTH1* IRE (11).

To date, IRE motifs have been found in a relatively small number of mRNAs. A canonical IRE structure is composed of a 6-nucleotide apical loop (5′-CAGWGH-3′, in which 'W' stands for A or U and 'H' for A, C, or U) on a stem of five paired nucleotides, a small asymmetrical bulge with an unpaired cytosine on the 5′-strand of the stem, and an additional lower stem of variable length. The nucleotides forming the two stem seg-

* This work was supported by the Marie Curie, Quality of Life Programme, CORDIS FP5 (Grant QLGA-CT-2001-52011) and the Young Investigator Award of the medical faculty Heidelberg, University of Heidelberg (to M. S.); by the Forschungsschwerpunktprogramm des Landes Baden-Württemberg, 2005 (RNA and disease) (to M. U. M. and M. W. H.); and by funds from the Gottfried Wilhem Leibniz Prize (to M. W. H.). The costs of publication of this article were defrayed in part by the payment of page charges. This article must therefore be hereby marked "*advertisement*" in accordance with 18 U.S.C. Section 1734 solely to indicate this fact.

[S] The on-line version of this article (available at http://www.jbc.org) contains supplemental Table S1 and Figs. S1–S3.

[1] To whom correspondence may be addressed. Tel.: 49-622-156-6923; Fax: 49-622-156-4580; E-mail: martina.muckenthaler@med.uni-heidelberg.de.

[2] To whom correspondence may be addressed. Tel.: 49-622-138-78501; Fax: 49-622-138-78518; E-mail: hentze@embl.de.

[3] The abbreviations used are: IRP, iron regulatory protein; IRE, iron-responsive element; CDC14A, cell cycle division 14 A; *SLC11A2*, solute carrier family 11 (proton-coupled divalent metal ion transporters), member 2 (or DMT1, divalent metal transporter 1); *TFRC*, transferrin receptor 1; *SLC40A1*, solute carrier family 40 (iron-regulated transporter), member 1 (or IREG1, iron-regulated gene *1*); *FTL*, ferritin light polypeptide; *FTH1*, ferritin heavy polypeptide; *ALAS2*, aminolevulinate Δ-synthase 2; SDH, succinate dehydrogenase; UTR, untranslated region; DFO, desferrioxamine; EMSA, electrophoretic mobility shift assay; EST, expressed sequence tag; RT, reverse transcription; qRT, quantitative real-time RT; mRNP, messenger ribonucleoprotein; IP, immunoprecipitation; SN, supernatant; wt, wild type; DRB, 5,6-dichloro-1-β-D-ribofuranosylbenzimidazole.

ments may vary considerably (12, 13). An algorithm was devised combining information on nucleotide sequence and RNA secondary structure to screen nucleotide databases for the presence of IRE-like motifs (14). Using this algorithm, we previously identified IREs in the 5′-UTR of *ALAS2* (15) and *Drosophila* succinate dehydrogenase mRNAs (16), showing the feasibility of using bioinformatics to identify novel IREs. However, *in vitro* selection procedures have yielded several IRE-like structures with alternative nucleotide composition, yet able to bind IRP1 and/or IRP2 (17–19). These data indicate that the primary nucleotide sequence of an IRP-binding IRE-like motif may vary considerably.

To explore the IRE/IRP regulatory network, we immunopurified IRP1/mRNA complexes formed with RNA isolated from various cell lines and tissues and identified novel IRP binding mRNAs using the IronChip cDNA microarray platform (20); here, the IronChip was complemented with genes bearing IRE-like motifs that we identified by bioinformatic screens of nucleic acid databases. We demonstrate that this integrated experimental strategy reliably identifies known IRE-containing genes, and we report the identification of a conserved IRE in the 3′-UTR of mRNA encoding the *CDC14A* tumor suppressor gene, pointing to a previously unrecognized regulatory link between iron metabolism and the cell cycle.

EXPERIMENTAL PROCEDURES

Cell Culture and Treatments—Cells were grown in 5% CO_2 at 37 °C in Dulbecco's modified Eagle's medium supplemented with 10% fetal bovine serum, 1% L-glutamine, 1% penicillin, and 1% streptomycin (HeLa, MCF7, HepG2, and 293 cell lines), or in RPMI 1640 medium supplemented with 10% fetal bovine serum, 1% penicillin, and 1% streptomycin (K562, THP1, and 786-O cell lines). Cells were treated with 100 μM desferrioxamine (DFO, Sigma), 100 μM hemin (Leiras Oy, Finland), or 100 μM ferric ammonium citrate (Sigma) for 10 h.

Mice—Animals were housed under a constant light/dark cycle in the EMBL SPF Mouse Barrier Unit. C57BL6/J females at weaning age were fed with a low iron (<10 mg/kg) diet (C1000, Altromin, Lage, Germany) for 3 weeks. Iron deficiency was assessed by decreased hematocrit (0.12 $\pm$ 0.03 liters/liter, $n = 3$, for mice fed with the iron-deficient diet compared with 0.31 $\pm$ 0.04 liters/liter, $n = 3$, for animals fed with the control diet) and hemoglobin values (7.6 $\pm$ 0.8 g/dl, $n = 3$, for mice fed with the iron-deficient diet compared with 12.8 $\pm$ 0.6 g/dl, $n = 3$, for animals fed with the control diet). Mice were sacrificed by CO_2 inhalation, and tissues were collected in RNAlater (Ambion) for subsequent RNA extraction. Animal handling was in accordance with institutional guidelines.

Plasmid Construction—Wild-type and mutant *FTH1* constructions for generating EMSA probes have been described previously (21). A human CDC14A IRE probe was generated by replacing the *FTH1* IRE sequence of the I-12. CAT plasmid (21) with synthetic oligonucleotides (Table S1) comprising the CDC14A IRE sequence. DNA templates were linearized with XbaI and used for *in vitro* transcription with T7 RNA polymerase.

RNA Extraction, Immunopurification of mRNPs, and Northern Blotting—Total RNA was extracted from cultured cells or mouse tissues using TRIzol (Invitrogen) according to the manufacturer's instructions. For immunopurifications, 50 μg of total RNA was denatured at 95 °C for 5 min and incubated with 2 μg of recombinant His-tagged IRP1 protein (21) for 10 min at 25 °C in immunopurification buffer IPP150 (10 mM Tris, pH 8.0, 150 mM NaCl, 0.1% Nonidet P-40) supplemented with 1% β-mercaptoethanol, 200 units of RNasin (Promega), and 200 units of Protector RNase Inhibitor (Roche Applied Science). Subsequently, 100 μl of 50% Protein A-Sepharose bead slurry (Merck) was added together with an affinity-purified rabbit polyclonal anti-IRP1 antibody raised against recombinant full-length human IRP1 (5), and the reactions were incubated for 30 min at 10 °C. Beads were washed twice in IPP150 buffer and treated with proteinase K prior to RNA extraction. RNA from the supernatant and the bead fractions was phenol-chloroform-extracted, ethanol-precipitated, and resuspended in water. Mouse liver and duodenal samples were studied by Northern blot analysis. One-fifth of the immunopurified RNA and one-third of the RNA present in the supernatant fraction were resolved on 1.2% formaldehyde-agarose gels and blotted onto nylon membranes (Nytran N, Schleicher and Schuell, Dassel, Germany). The membranes were then hybridized to ^{32}P-labeled DNA probes in Church Buffer (0.5 M sodium phosphate, pH 7.2, 7% w/v SDS, 1 mM EDTA, pH 8.0) (22). Radiolabeled DNA probes were generated by random primer labeling (High Prime, Roche Applied Science) of purified PCR products obtained from cDNA clones of the following mouse genes: *Tfrc*, *Slc40a1* or Ireg1, *Ftl*, *Fth1*, *β-actin*, and *Gapdh*. The signals obtained were quantified using a PhosphorImager (Fujifilm FLA-2000, Amersham Biosciences).

Computer-assisted Identification of Putative IREs—Human, mouse, and rodent sections of the EMBL data base (version 77) were screened for the presence of IRE-like motifs combining sequence and RNA fold energy criteria, as described previously (14). For 5′-UTR IRE motifs, the search was restricted to sequences located within the first 200 nucleotides of the mRNA leader; for 3′-UTR IRE motifs, only sequences conserved in at least two species were selected.

Additionally, we screened a list of 230 IRE-like sequences that were retrieved from the UTR data base (version from October, 2004, available at www.ba.itb.cnr.it/UTR/) (23). These putative IRE sequences match the PatSearch Pattern defined for the ferritin or *TFRC* IRE model sequences (23). After subtracting known IRE mRNAs, 141 putative IRE sequences remained. From these, we selected those that closely resemble an IRE structure with a lower stem containing at least six out of seven paired nucleotides. Only six IRE-like motifs remained after imposing this criterion (Table 1).

Microarray Experiments—Human and murine cDNA clones corresponding to genes retrieved from the biocomputational search for IRE-like structures (see Table 1 for a full list of these genes) were spotted onto the human or mouse "IronChip" microarray platform, respectively. 48 human EST sequences corresponding to 18 genes (out of 21) were spotted onto the human IronChip microarray platform (versions 4.0 and 5.0 (20)), and 39 mouse EST sequences corresponding to 16 genes

(out of 21) were spotted onto the murine IronChip microarray platform (versions 5.0, 6.0, and 7.0 (24); see www.embl.de/iron-systems/IronChip_genes.html for updated versions of the IronChip). For IronChip analyses, 5 μg of total RNA was reverse-transcribed, amplified, and labeled as described previously (20).

RT-PCR Experiments (qRT-PCR and Semiquantitative RT-PCR)—Total RNA was extracted from 293 cells, and 2 μg was used for first strand cDNAs synthesis with random primers and Superscript II reverse transcriptase (Invitrogen) according to the manufacturer's instructions. Quantitative real-time RT-PCR (qRT-PCR) was performed using SYBR green and an ABI 7500 sequence detection system instrument and software from Applied Biosystems. The data represent the average of three independent tissue culture experiments for which qRT-PCR analyses were performed in duplicate. mRNA expression ratios in DFO-treated *versus* control cells (untreated) were calculated using the comparative Ct method with correction for amplification efficiencies as described previously (25); values were normalized to β-actin mRNA levels. For qRT-PCR analysis of IRP/IRE mRNPs, 65 ng of immunopurified RNA from 786-O cells was reverse transcribed. mRNA levels were determined for three independent immunopurified experiments for which each qRT-PCR analysis was done in triplicate. For semiquantitative RT-PCR one-fifth or three-fifths of the RT sample, depending on mRNA abundance, was used for PCR amplification with *Taq* Platinum (Invitrogen) after RNase H treatment. The amplification was performed at 95 °C for 30 s, 55 °C for 30 s, and 72 °C for 2.5 min for 16, 23, or 35 cycles depending on the concentration of the cDNA (β-actin, *TFRC*, or CDC14A, respectively). The PCR products were resolved on 1% ethidium bromide-stained gels where the predicted amplification product size was observed. For each set of primers, the number of PCR cycles was optimized for linearity of the reaction. Primers spanning the four different isoforms of CDC14A mRNA (1A-IRE, 1B-IRE, 1A-non-IRE, and 1B-non-IRE) were used under C, control (no treatment); H, hemin; D, DFO; or −RT, no RT enzyme added conditions. β-Actin and *TFRC* mRNAs were amplified as negative and positive controls for iron regulation, respectively. The primers used for the analysis are listed in supplemental Table S1.

Electrophoretic Mobility Shift Assay—Gel-retardation analyses were performed as described previously (26). Briefly, a [^{32}P]UTP-labeled human *FTH1* IRE probe (600,000 cpm) was incubated with 10 ng of purified recombinant His-tagged IRP1 or IRP2 protein (21) for 15 min at 25 °C in the presence of increasing molar excess of unlabeled competitor probes. Nonspecific RNA-protein interactions were displaced by the addition of 50 μg of sodium heparin for 10 min. Supershift experiments were performed by adding immunopurified rabbit polyclonal anti-IRP1 or anti-IRP2 antibodies (5) for 10 min. RNA-protein complexes were resolved by nondenaturing PAGE and visualized using a PhosphorImager (Fujifilm FLA-2000, Amersham Biosciences).

RESULTS

Strategy to Identify Novel IRE-containing mRNAs—To identify novel IRE-containing mRNAs we combined biochemical and biocomputational approaches coupled with microarray

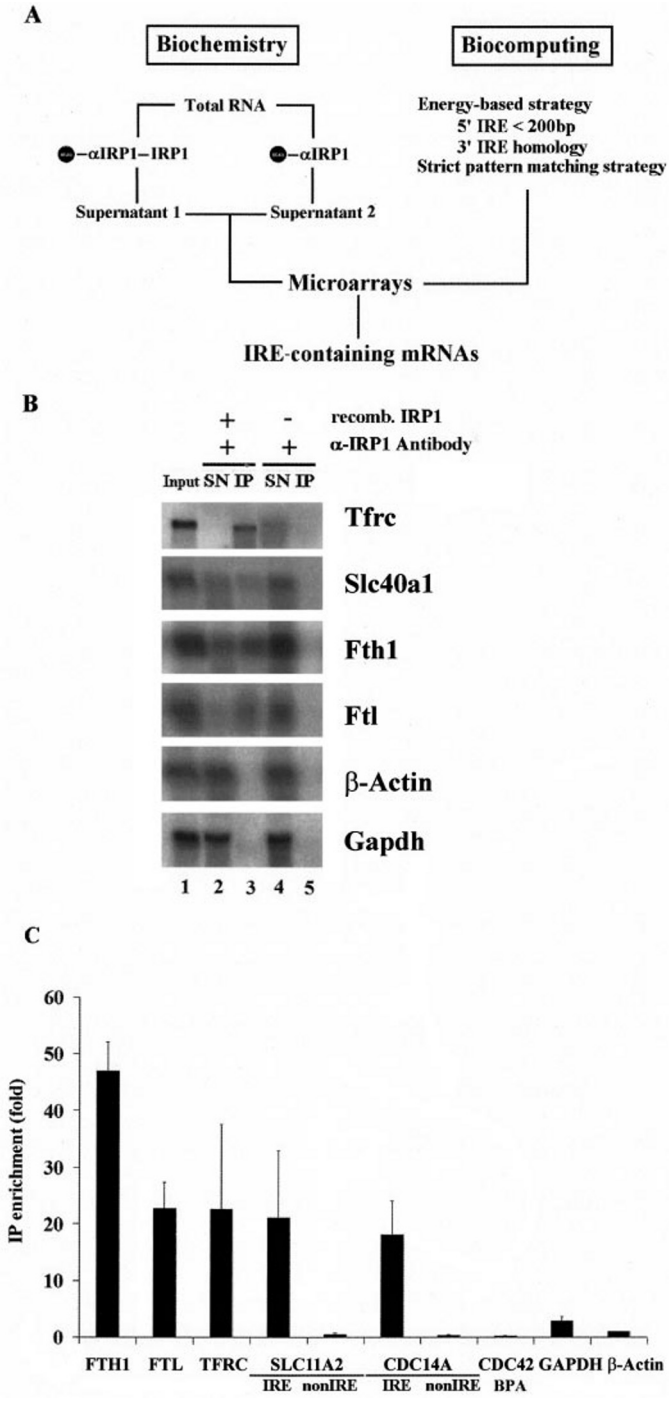

FIGURE 1. **Experimental strategy, immunoselection, and characterization of IRP/IRE mRNPs.** *A*, biochemical and biocomputational approaches converge in microarray analyses for the identification of novel IRE-containing genes. IRP/IRE mRNPs were isolated using anti-IRP1 antibodies and recombinant IRP1. Immunodepletion of IRE-containing mRNAs from the supernatant was analyzed using microarrays. Nucleic acid databases were screened for IRE-like motifs using several biocomputational approaches and restriction filters. The identified genes were spotted onto the IronChip microarray platform. The specificity and efficiency of IRP/IRE mRNP isolation was tested by Northern blot analysis of supernatant (*SN*) and immunopurified (*IP*) fractions (*B*), and by qRT-PCR analysis of IP samples (*C*). β-Actin and glyceraldehyde-3-phosphate dehydrogenase mRNAs were used as negative controls in Northern blot experiments (*B*). The histogram (*C*) shows ratios (mean ± S.D.) of mRNA levels (normalized to β-actin mRNA) in IP fractions obtained in the presence *versus* absence of recombinant IRP1.

TABLE 1
Summary of IRE-like motifs identified biocomputationally

Gene name	Ref. sequence	Specie	IRE at	IRE sequence	IRE in other species	E IRE[a]
ADAR	NM_001111	*H. sapiens*	5′	GCCCCGGGGC.C.ACUUC.CAGUGC.GGAGUAGCGGAGGCGUG	*D. melanogaster*	−12.9
PRKACA	NM_002730	*H. sapiens*	5′	GCCUUCCCAG.C.CACCG.UAGUGC.CGGUGCCCUGAGAACAG	*M. musculus*	−10.4
Rnf5	NM_019403	*M. musculus*	5′	UGUGUGUGCC.C.UGUGU.UAGUGU.AUAUGUGUGUGUGCCUG	*H. sapiens*	−3.8
S6K[b]	NM_079217	*D. melanogaster*	5′	GUGCGUG.C.CGUCG.CAGUGU.UGGUGCGUGUGC		−9.0
Sh3gl3	NM_017400	*M. musculus*	5′	GCGCGCGCGC.C.UGUGC.CAGUGU.GACAGCGCCGUGGCCGU	*H. sapiens*	−13.1
BRF1[b]	NM_001519	*H. sapiens*	3′	GCAGGGG.C.CGGUG.CAGAGC.CACUG.UCUGUGU		−9.9
CAV3	NM_001234	*H. sapiens*	3′	CUUGGGCUGG.C.AGGGG.CAGUGA.CCCUUCCAGGGU	*M. musculus*	−13.1
CDC14A[b]	NM_003672	*H. sapiens*	3′	AUAUUUA.C.AUGUA.CAGUGU.UACAUUAUAUAU	*M. mulatta, B. taurus,* and *R. norvegicus*	−1.4
CDC42BPA[b]	NM_003607	*H. sapiens*	3′	UAGAAAA.C.ACUUG.CAGAGC.CAGGU.UUUGCUG		np[c]
Cnbp1	NM_013493	*M. musculus*	3′	GAGGCUGUUC.C.CAGGC.CAGUGA.GCUUUACUUGCAGUGUA	*H. sapiens* and *R. norvegicus*	−8.3
D11Ertd498e	NM_145940	*M. musculus*	3′	GAGUUUGCGA.C.GGGAC.CAGUGU.GUCUAGACGACGAGAAU	*H. sapiens*	−6.3
DKFZP564B147	AL117556	*H. sapiens*	3′	GGACACAGCC.C.CUGGA.CAGUGA.UCCAGACAGCUGGCCGU	*M. musculus*	−14.4
Dsipi	NM_031345	*R. norvegicus*	3′	CCUAGUAACC.C.CAAGC.CAGUGA.GCUUGUCGUGCCACCGG	*H. sapiens* and *M. musculus*	−7.0
FLJ34594[b]	XM_379386	*H. sapiens*	3′	GAGCUCC.C.UGACC.CAGAGA.GGUUA.AGGGUUU		−9.0
FLJ44675[b]	AK126633	*H. sapiens*	3′	GAAGAUU.C.UUUGG.CAGUGU.CCAAGAAUUAUC		−5.9
PSMA4	X91847	*S. scrofa*	3′	AUUUGGGGCA.C.CAGUU.CAGUGU.AAAAGCUGUCCUACUCU	*H. sapiens*	−6.3
SERTAD2	NM_014755	*H. sapiens*	3′	UAGUUUUUGC.C.UUUUU.CAGAGA.AAAAGAAAUUGCUUUGA	*M. musculus*	−3.8
SMARCC2	NM_003075	*H. sapiens*	3′	CCCUGUGC.C.ACCUC.CACAGU.GAGGAGCCAGCCAGACAUC	*M. musculus*	−9.9
TRAM1	NM_014294	*H. sapiens*	3′	CUGUUUGUGC.C.AUUUU.UAGUGU.AAAAGUUGCAGACCUAU	*C. familiaris*	−4.7
Vdac3	NM_011696	*M. musculus*	3′	AUAUCAGUCU.C.UGCUC.UAGUGA.GAGCUUUGGUUUUGCAU	*H. sapiens*	−6.3
ZC3H11A/ KIAA0663	NM_014827	*H. sapiens*	3′	UAGAGGAAUU.C.UUUUU.UAGUAU.GAAAAUUGUCCCUUUUC	*M. musculus*	−5.2

[a] E, predicted IRE structure energy (14).
[b] IRE-like motifs selected from the UTRdb (23).
[c] np, not possible to determine.

analysis (Fig. 1*A*). In this approach, IRP/IRE mRNPs were immunoselected, and their mRNA composition was analyzed using microarrays. The experimental strategy was validated using the IronChip (16), a specialized cDNA microarray platform established to study iron metabolism-related genes. The IronChip contains all known IRE genes and was complemented here specifically with cDNAs predicted to bear IRE-like sequences (see below).

Immunopurification of IRP/IRE mRNPs—Total RNA from different sources was incubated with recombinant human IRP1 followed by immunoselection of IRP1/IRE mRNPs with an affinity-purified polyclonal rabbit anti-IRP1 antibody raised against full-length human IRP1 (5); in control reactions, the addition of recombinant IRP1 protein was omitted (Fig. 1*A*). In preliminary experiments, we had optimized the specificity and the yield of the procedure in terms of incubation conditions and amount of added recombinant IRP1, using radiolabeled *in vitro* transcribed reporter mRNAs bearing wild-type (positive control) and mutant (negative control) *FTH1* IRE (data not shown). The input RNA was extracted from different human cell lines (HepG2: hepatoma, Caco-2: colon adenocarcinoma, HeLa: cervix adenocarcinoma, MCF7: breast adenocarcinoma, K562: erythroleukemia, TPH1: myeloid leukemia, 293: embryonic kidney cells, and 786-O: renal adenocarcinoma) and mouse tissues (liver, spleen, brain, duodenum, heart, lung, and kidney). Prior to RNA extraction, mice and cell lines were made iron-deficient to increase the abundance of IRE-containing mRNAs like the *TFRC* and *SLC11A2* (DMT1) mRNAs. Following optimization, the efficiency and the specificity of the immunoselection procedure were confirmed by testing the levels of four known IRE-containing mRNAs (*Tfrc*, *Slc40a1* or Ireg1, *Ftl* or ferritin light polypeptide, and *Fth1* or ferritin heavy polypeptide 1) as positive controls together with negative controls in the immunoprecipitated (IP) and in the supernatant (SN) fractions by Northern blotting. As shown in Fig. 1*B*, all four positive control mRNAs were significantly enriched in the IP fraction (compare *lanes 3* and *5*) and depleted from the SN fraction (compare *lanes 2* and *4*) in an IRP1-dependent, specific manner. The degree of depletion from the SN varied among the four mRNAs, with a more effective depletion of the *Tfrc* and the *Fth1* and *Ftl* mRNAs than the *Slc40a1* mRNA. This difference may arise from the hierarchy of affinities of the IRE-containing mRNAs for IRP1. Importantly, negative control mRNAs devoid of IRE motifs (β-actin and glyceraldehyde-3-phosphate dehydrogenase) were neither enriched in the IP fraction nor depleted from the SN (see *lanes 2* and *3*, Fig. 1*B*).

Because *SLC11A2* isoforms (IRE *versus* non-IRE) cannot be distinguished by Northern blotting, we also analyzed the IP fractions from three independent experiments by qRT-PCR. In agreement with the Northern blot data (Fig. 1*B*) the *FTH1* and *FTL* mRNAs, as well as the *TFRC* mRNA, were strongly enriched in the IP fraction (46.9 ± 5-fold, 22.7 ± 5-fold, and 22.6 ± 15-fold, respectively) (Fig. 1*C*). In addition, the *SLC11A2*-IRE mRNA isoforms were selectively enriched in the IP fraction (21.0 ± 12-fold), whereas the non-IRE isoforms expectedly behaved as negative control (0.4 ± 0.4-fold) confirming the high selectivity and specificity of the procedure. Taken together, these data show that the immunoselection strategy efficiently and selectively isolates IRE-containing mRNAs.

Biocomputational Identification of Novel IRE-like Motifs—IRE-like motifs were identified from genomic nucleic acid databases by an algorithm combining primary nucleic acid sequence and RNA structural criteria (14, 23). Depending on the choice of constraining criteria, such computational screens tend to generate a large number of false positives. To refine the

A

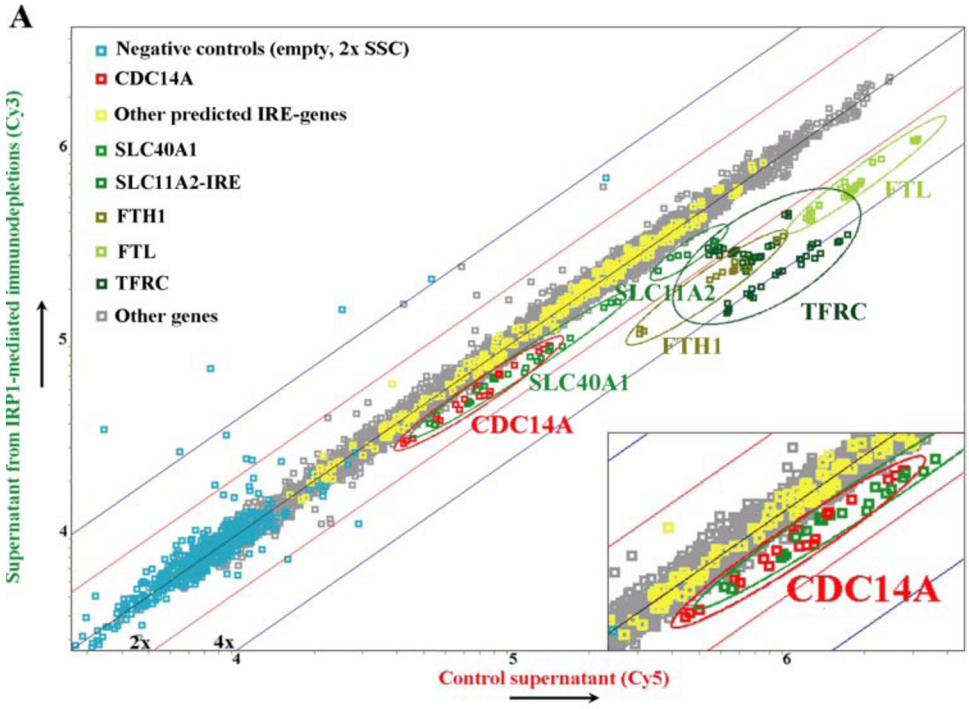

B

Mouse tissues	Gene *TFRC*	*FTL*	*FTH1*	*SLC40A1*	*SLC11A2*	*CDC14A*
Liver	+++	+++	+++	n.a.		
Spleen	++	++	+++			
Brain	++	+	++	n.a.	(+)	
Duodenum	++	+	++	+	(+)	
Heart	+++	+++	++++	n.a.		
Lung	++	++	++	n.a.	(+)	
Kidney	+++	+++	+++	n.a.		

Human cell lines	Gene *TFRC*	*FTL*	*FTH1*	*SLC40A1*	*SLC11A2*	*CDC14A*
HepG2 (liver)	+	+	+	(+)		
Caco-2 (intestine, colon)	+++	++	++	+	(+)	
HeLa (uterus cervix)	+++	++	+			
MCF7 (breast)	++	+	+		(+)	
K562 (blood)	+	+	+			
TPH1 (bone marrow)	++	+	+			(+)
293 (kidney)	++	+	(+)			(+)

FIGURE 2. **Microarray analysis detects known IRE-regulated mRNAs and identifies the novel IRE-containing gene CDC14A.** The depletion of IRE-containing mRNAs from the SN fractions (*cf.* Fig. 1*A*) was analyzed using a dual color cDNA microarray analysis (IronChip). *A*, virtual scatterplot generated from Caco-2 and 293 human cell line data. Known IRE-regulated genes are represented by *green dots* and predicted IRE-genes by *red* or *yellow dots*. Known IRE-regulated genes and CDC14A are *circled*. The 2-fold and 4-fold depletion limits are indicated by *red* and *blue lines*, respectively. *B*, summary of the data obtained from all mouse tissues and human cell lines analyzed in this study. The -fold depletions are indicated as follows: +, >1.4; ++, >2.0; +++, >3.0; and ++++, >4.0. (+) indicates that not all ESTs represented on the IronChip microarray platform performed as expected in dye switch experiments. *n.a.*, the corresponding gene was not available on the microarray version used.

search and reduce the number of false positive hits, additional constraints were introduced. First, we restricted the positive hits to those whose IRE folding energy was consistent with the energy of known IREs (at least −3 kcal/mol or below). In addition, putative 5′-IRE motifs had to be located within the first 200 nucleotides of the mRNA leader, because the distance between functional 5′-IREs and the cap structure has been shown to be critical for efficient translational repression in mammals (27). Such criteria identify all known 5′-IREs, including the experimentally confirmed IRE in *SLC40A1* (28). For 3′-IRE motifs, only those conserved in at least two different species were selected. This refined screen yielded 15 IRE motifs (4 within the 5′-UTR and 11 within the 3′-UTR) (Table 1). A second approach made use of a reported list of 230 IRE-like sequences obtained from screening UTR databases (23). We selected 6 out of these 230 entries based on the ability of the lower IRE stem to form at least 6 out of 7 bp (Table 1). Thus, 21 mRNAs with IRE-like motifs were selected in total. Corresponding ESTs were spotted onto the human or mouse versions of the IronChip, a sensitive cDNA microarray platform covering ~500 genes involved in iron metabolism and connected metabolic pathways (*e.g.* copper and oxygen metabolism) (20).

IronChip Analysis of IRP/IRE mRNPs—To determine whether mRNAs with biocomputationally predicted IRE-like motifs are contained within the immunopurified IRP/IRE mRNPs, we extracted their mRNAs for analysis on IronChips that include all known IRE-containing genes as well as those genes with IRE-like motifs identified by the biocomputational strategy (see above).

Because the complexity of the mRNA population in the immunopurified (IP) fraction is not sufficient for global normalization protocols applied to dual color microarray data analyses (29), we used the supernatant (SN) fractions that offer high mRNA complexity and assayed these for the depletion of IRE-containing mRNAs. To exclude possible artifacts associated with uneven incorporation of cyanine dyes into cDNAs, we routinely performed dye switch experiments (29).

The reduction of known IRE-containing mRNAs (positive controls) from specific IRP1-mediated immunodepletions was clearly observed in the case of the *TFRC* mRNA and the *FTH1*

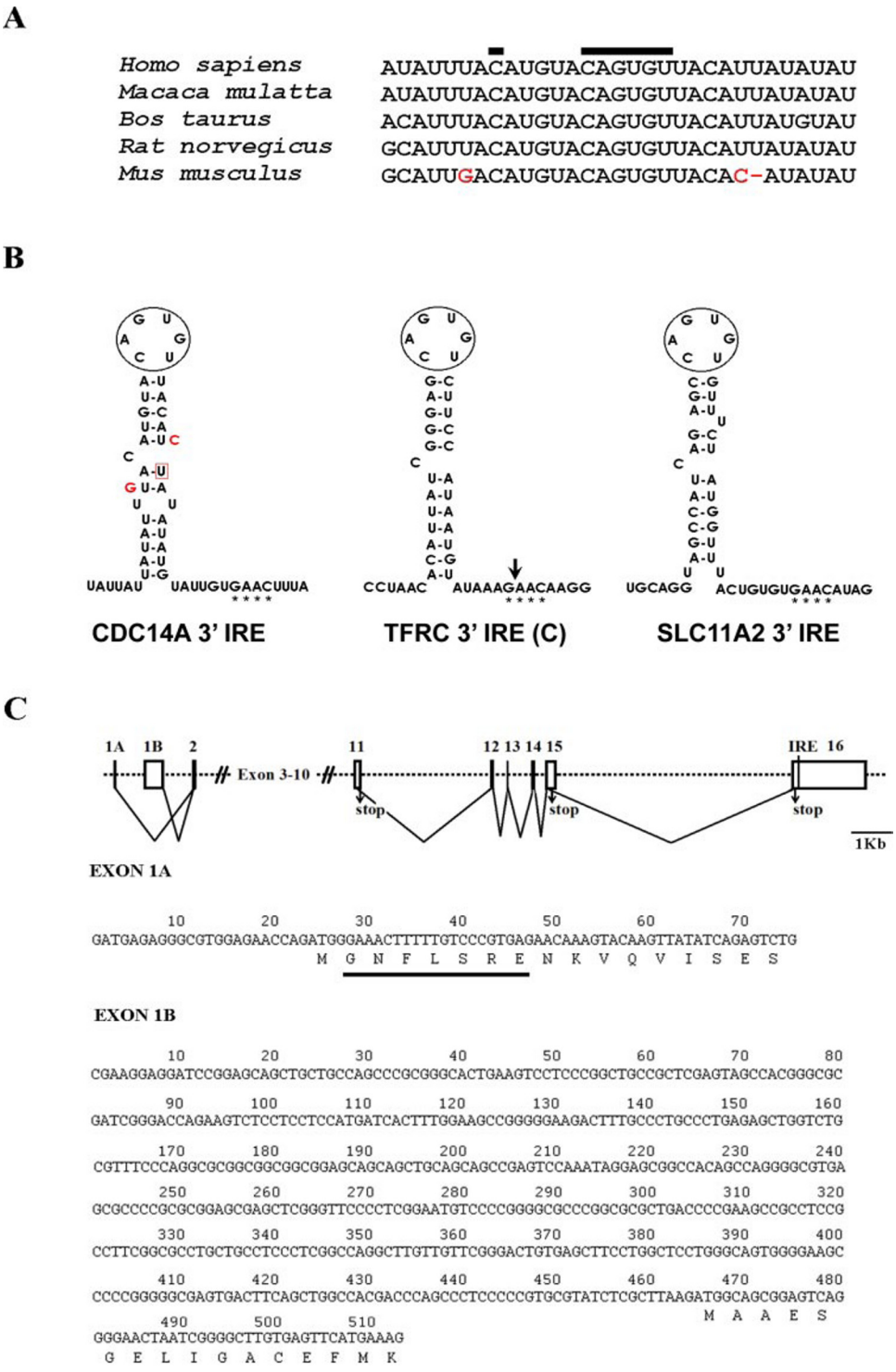

FIGURE 3. **Structure and phylogenic conservation of the CDC14A 3′-UTR IRE and genomic organization of the human CDC14A gene locus.** *A*, phylogenic conservation of the CDC14A mRNA IRE. The C-bulge and the IRE loop are indicated with *black lines*. *B*, representation of the IRE structures present in the 3′-UTR of the human CDC14A, *TFRC*, and *SLC11A2* mRNAs. Nucleotides disrupting the IRE structure in the mouse sequence are indicated in *red* in (*A*) and (*B*). The proposed endonucleolytic cleavage site in the *TFRC mRNA* is indicated by an *arrow*; a conserved four-nucleotide sequence is marked with *asterisks*. In *C*: *Top*, genomic organization of the human CDC14A locus; the stop codons and the IRE sequence are indicated. *Bottom*, nucleotide and amino acid sequences corresponding to the novel exon 1A and of the previously described exon 1B (*lower part*); the putative *N*-myristoylation site in exon 1A is *underlined*.

and *FTL* mRNAs in all tissues and cell lines tested (Fig. 2, *A* and *B*). The tissue-specific *SLC40A1* or IREG1 mRNA was detected in RNA samples of mouse duodenum and human Caco-2 cells and efficiently depleted from these input RNAs by an immunoselection procedure. Depletion of the *SLC11A2*-IRE (DMT1) mRNA was detectable in RNA from mouse duodenum, lung, and brain as well as human Caco-2 and MCF7 cell lines. The other tested tissues and cell lines did not detectably express *SLC11A2* mRNA. The IronChip analysis therefore nicely mirrored the data generated by Northern blotting (Fig. 1*B*) and qRT-PCR (Fig. 1*C*) and thus is a suitable tool to identify *bona fide* IRE-containing mRNAs in the supernatant fractions of IP reactions.

From the 21 candidates that were selected biocomputationally, the majority was either undetectable or not significantly depleted from the SN fraction. These data are in agreement with qRT-PCR analyses showing a lack of enrichment of the CDC42BPA mRNA and additionally tested biocomputational candidate mRNAs (Fig. 1*C* and data not shown). Of note, the CDC14A mRNA was efficiently depleted from the supernatant of two human cell lines (293 and TPH1) (Fig. 2) and enriched in the immunopurified IRP1/IRE mRNPs from the human cell line 786-O (see Fig. 1*C*). Taken together, these data show that the immunoselection/microarray strategy is a feasible approach for screening bioinformatically predicted IRE genes and the detection of novel IRE-containing mRNAs.

Characterization of the Human CDC14A mRNA—To further characterize the human CDC14A IRE sequence, we analyzed its phylogenetic conservation and investigated the genomic organization of the human *CDC14A* gene.

The CDC14A IRE sequence is located in the 3′-UTR and is conserved in multiple mammalian species (human, monkeys, bull, and rat) (Fig. 3*A*). Unexpectedly, murine CDC14A mRNA bears an IRE sequence that is altered, with a U → G conversion affecting the lower stem, and a C replacing a U in the final position of the 3′-strand of the upper stem followed by a single nucleotide deletion (Fig. 3*B*, *red nucleotides*). All theses substitutions alter the predicted

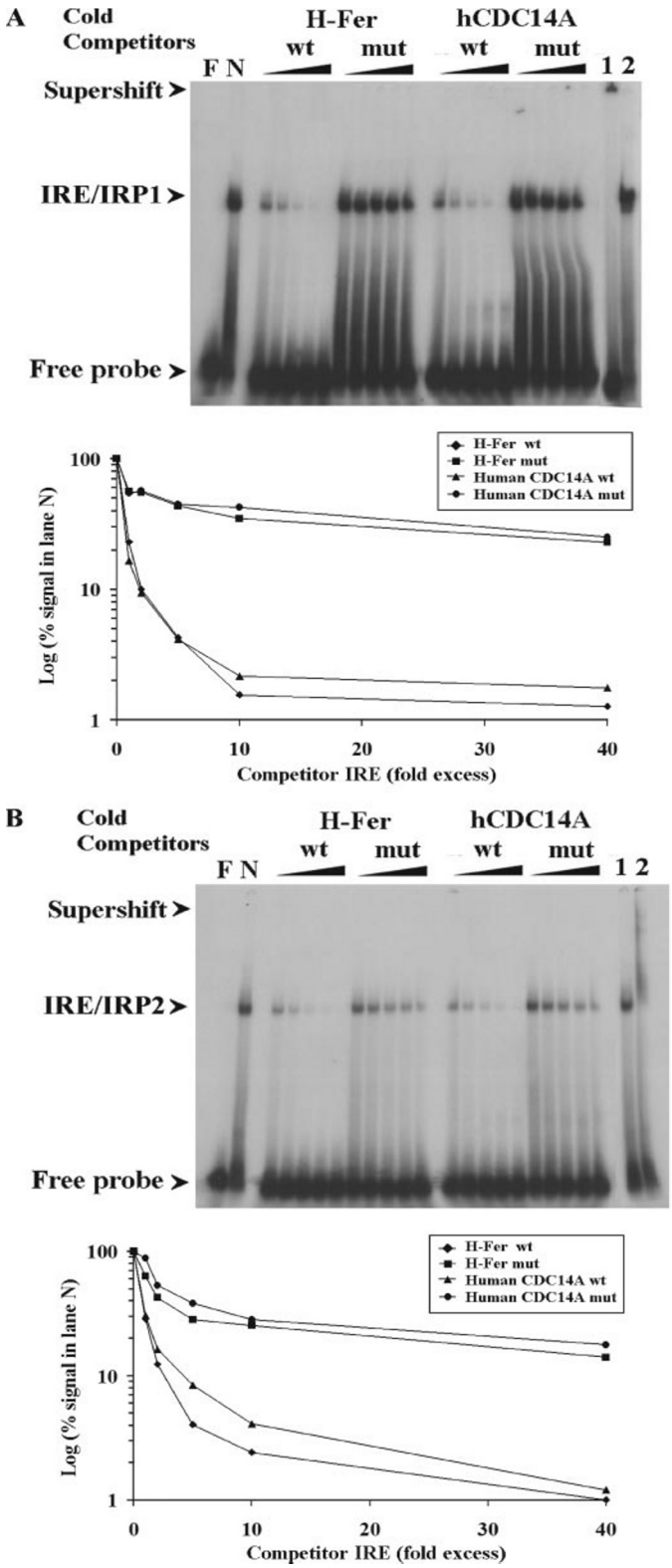

FIGURE 4. **The CDC14A IRE efficiently binds to IRP1 and IRP2.** The binding of the human CDC14A IRE by recombinant IRP1 (*A*) or IRP2 (*B*) was studied by competitive EMSA using a ^{32}P-labeled *FTH1* IRE probe and an increasing molar excess of cold competitor RNAs: *FTH1* (*H-Fer*) wild type (*wt*); *FTH1* ΔC mutant (*mut*); human CDC14A (*hCDC14A*) wt, and ΔC mutant (*mut*). The intensity of the shifted signal was quantified using a phosphorimaging system. Data are represented below the autoradiographs. *F*: free probe, *N*: no competitor added, *1* and *2*: supershift experiments with rabbit anti-IRP1 or anti IRP2-polyclonal antibodies, respectively.

structure of the IRE and abrogate IRP binding to the mouse IRE (supplemental Fig. S1). Comparison of the human CDC14A IRE locus with the previously identified 3′-UTR IRE sequences of *TFRC* and *SLC11A2* reveals four conserved nucleotides (GAAC) downstream of the IRE loci, corresponding to the reported endonucleolytic cleavage site in the *TFRC* 3′-UTR (30, 31) (Fig. 3*B*, *arrow*). However, the flanking regions surrounding the GAAC sequence are not well conserved among CDC14A, *TFRC*, and *SLC11A2*, but may be functionally important.

A GenBank™ data base search revealed the existence of three alternative splice variants of the human CDC14A mRNA, which diverge in their 3′-end (variant 1 [NM_003672], variant 2 [NM_033312], and variant 3 [NM_033313]). The IRE motif is located in exon 16 of variant 1 mRNA, 301 nucleotides downstream from the stop codon (Fig. 3*C*). In addition, we identified an additional alternative 5′-splice variant by EST alignments (Fig. 3*C*), which includes a novel exon (exon 1A) located 682 bp upstream of the reported first exon (exon 1B). Exon 1A is predicted to encode an alternative N-terminal sequence of 17 amino acids containing a putative *N*-myristoylation site (Fig. 3*C*, *underlined*).

Human CDC14A IRE Binds IRPs—We next characterized the binding characteristics of the CDC14A IRE to IRP1 and IRP2 by competitive EMSAs. In this assay, a ^{32}P-labeled *FTH1* IRE probe is incubated with either recombinant IRP1 or IRP2 and an increasing amount of unlabeled IRE competitors. Supershift experiments with specific anti-IRP1 or -IRP2 antibodies were performed to demonstrate the specificity of the observed IRP-IRE interactions. As expected, the unlabeled wild-type (wt) *FTH1* IRE RNA transcript competes efficiently for the binding of the ^{32}P-labeled ferritin *FTH1* IRE probe to both IRPs, whereas a mutated negative control competitor (mut), consisting of a ΔC mutation in the IRE loop (16), did not (Fig. 4, *A* and *B*). The CDC14A IRE competitor displayed a similar behavior with efficient competition by the wt CDC14A IRE motif, which was abolished by an analogous ΔC mutation. Using extracts from mouse Ltk fibroblasts we confirmed that the CDC14A IRE specifically binds both IRPs (data not shown), demonstrating that the CDC14A IRE efficiently binds both recombinant and endogenous IRPs.

CDC14A IRE mRNA Is Specifically Regulated by Iron Deficiency—Finally, we assessed whether the CDC14A mRNA is regulated by iron levels in human 293 cells. Cells were treated with either 100 μM iron chelator (DFO, Fig. 5) or with 100 μM hemin or ferric ammonium citrate as iron sources (supplemental Fig. S2) and were harvested after 0, 10, and 20 h of treatment. The mRNA levels of the CDC14A 3′ splice variants (IRE *versus* non-IRE isoforms) were measured separately by qRT-PCR using specific primers. As a positive control for iron regulation, we monitored *TFRC* mRNA levels in the same samples. As expected, *TFRC* mRNA expression was increased upon DFO treatment and diminished upon iron treatment (Fig. 5 and Supplemental Fig. S2) (32). Similar to *TFRC*, the expression of the CDC14A-IRE mRNA isoforms were selectively increased in iron-deficient cells, whereas the levels of the CDC14A-non-IRE variants remain unchanged (Fig. 5). Unlike *TFRC*, the levels of CDC14A mRNA isoforms (with or without the IRE motif)

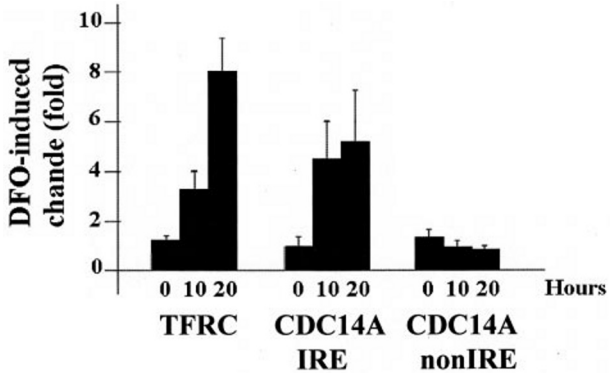

FIGURE 5. **CDC14A IRE mRNA levels are increased in iron-deficient cells.** 293 cells were treated with 100 μM DFO. *TFRC*, CDC14A-IRE, and CDC14A-non-IRE mRNA levels were assayed by qRT-PCR at 0, 10, and 20 h after treatment. For each time point, data were normalized to β-actin mRNA levels. The histograms represent expression levels in DFO-treated *versus* control cells (-fold change). Data were generated from three independent biological repeats, and qRT-PCR experiments were performed in duplicate. Data are presented as mean ± S.D.

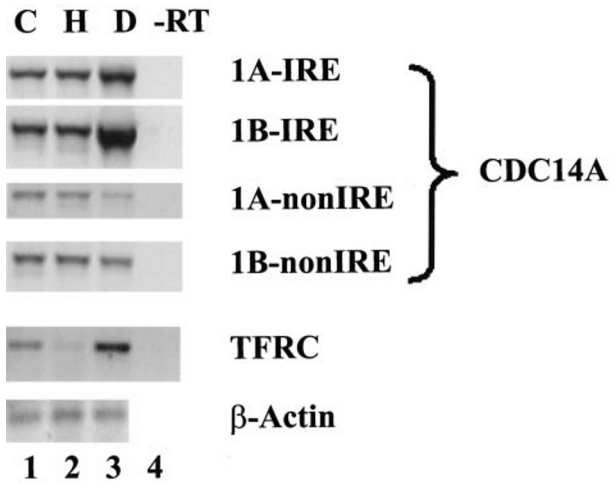

FIGURE 6. **IRE-specific iron regulation of the 1A-IRE and 1B-IRE isoforms of CDC14A mRNA.** 293 cells were treated with 100 μM DFO or hemin or left untreated for 10 h. mRNA levels for *TFRC*, β-actin, and the four different isoforms of CDC14A (1A-IRE, 1B-IRE, 1A-non-IRE, and 1B-non-IRE) were assessed by semiquantitative RT-PCR. *C*, control (untreated); *H*, hemin; *D*, DFO; *-RT*, RNA sample from *lane 4* with no RT added. β-Actin and *TFRC* mRNAs were amplified as negative and positive controls for iron regulation, respectively. Experiments were done in triplicate, and one representative result is shown.

are not significantly affected by elevated cellular iron levels (supplemental Fig. S2).

As detailed in Fig. 3*C*, four CDC14A mRNA isoforms appear to be generated by the combination of alternative 5′and 3′ splicing events (1A-IRE, 1A-non-IRE, 1B-IRE, and 1B-non-IRE). We analyzed the expression of these four variants by semiquantitative RT-PCR using primers spanning the complete mRNA sequence. We observed a selective up-regulation of the 1A- and 1B-IRE variants by cellular iron deficiency, distinct from the non-IRE isoforms (Fig. 6). These data show that the CDC14A mRNA isoforms containing the 3′-IRE are selectively regulated by iron deficiency, independent of whether transcription initiates at exon 1A or exon 1B.

The 3′-UTR IREs of the *TFRC* mRNA have been shown to mediate mRNA stabilization upon IRP binding (33, 34). To implicate a similar mechanism in the regulation of CDC14A-IRE mRNA isoforms we determined their turnover rates in 293 cells treated with DFO and the transcription inhibitor 5,6-dichloro-1-β-D-ribofuranosylbenzimidazole (DRB). Compared with control samples, the *TFRC* mRNA half-life is detectably prolonged following DFO treatment, as expected (supplemental Fig. S3). However, the small change observed in CDC14A-IRE mRNA turnover under the same conditions was not significant (supplemental Fig. S3). Although the 3′-UTR position of the IRE and the specific regulation by iron deficiency as well as the conservation of the putative *TFRC* RNA cleavage site are suggestive, the available data do not allow to conclude at present that the regulatory mechanism of the CDC14A-IRE mRNA resembles that of *TFRC*.

DISCUSSION

Early embryonic lethality in mice deficient for both IRP1 and IRP2 shows that the IRP/IRE regulatory network is vital (9). Indeed, IRPs regulate the expression of genes that are essential for iron homeostasis (*e.g.* ferritins and *TFRC*). Because the number of mRNAs that have been shown to be regulated via IREs is relatively small, we addressed the question of whether yet unidentified IRE-containing mRNAs exist. In a previous study, Kohler *et al.* (35) found an IRE-like motif in the mouse glycolate oxidase (*GOX*) gene, which did not confer iron-dependent regulation in cells. Here we describe a novel strategy that combines biocomputational, biochemical, and microarray-based approaches and that identifies a novel IRE in the human CDC14A mRNA. This discovery suggests that previously unrecognized genes belong to the IRE/IRP regulatory network and points to a previously unrecognized molecular link between iron metabolism and the cell cycle.

Screening for New IRE-containing mRNAs—An IRE motif is characterized by a 6-nucleotide apical loop with the consensus sequence 5′-CAGWGH-3′ on an upper stem of 5 bp, a small asymmetric bulge with an unpaired cytosine and an additional lower stem of variable length. We performed a biocomputational screen for IRE-like motifs, including restricted search criteria to minimize the number of false positives. Nonetheless, most of the 21 candidate mRNAs could not be detected in immunoselected IRP/IRE mRNPs when assessed by IronChip or qRT-PCR in RNA samples from several sources. Possible reasons for falsely negative results include the lack of expression of these mRNAs in the cell types or tissues tested, the masking of an IRE-containing isoform by more abundant non-IRE splice variants, or the exclusive binding to IRP2 instead of IRP1. Therefore, we characterized the binding of some of these predicted IREs to IRP1 (11 candidates tested) or IRP2 (6 candidates tested) using competitive EMSA. With the notable exception of the human CDC14A IRE, none of the tested IRE candidates was able to compete efficiently for IRP1 or IRP2 binding to the *FTH1* IRE probe (Supplemental Fig. S1). These data clearly suggest that many of the IRE-like motifs identified by the biocomputational screen possess low IRP binding affinity.

Previous biocomputational IRE motif searches included primary RNA sequence information and RNA folding criteria consistently guided by the folding energy of known IREs (at least −3 kcal/mol or below) (15). These searches missed the CDC14A IRE (−1.4 kcal/mol; Table 1) that was identified here

using a search algorithm that excluded energy requirements (23). This so-called "pattern search algorithm" also identified an IRE-like motif in the CDC42BPA (MRCKα) mRNA, which was recently reported to be iron-regulated by Cmejla *et al.* (36). However, this mRNA was not detected in our immunoselections using recombinant IRP1 (Fig. 1*C*), and the CDC42BPA IRE motif displayed poor IRP1 and IRP2 binding in competitive EMSA (Supplemental Fig. S1). We also did not observe significant iron regulation of the CDC42BPA mRNA in 293 cells (data not shown). In contrast, Cmejla *et al.* observed a marginal increase of CDC42BPA mRNA levels in Hep3B cells treated with DFO (36).

Future studies to further explore the IRE/IRP regulatory network will use the immunoselection procedure described here in combination with whole genome microarrays and/or recombinant IRP2. Because mRNAs exist in various splice variants, including IRE and non-IRE isoforms (*e.g. SLC11A2* and CDC14A), the relative abundance of non-IRE variants can potentially interfere with the detection of IRE variants in microarray experiments. Here we used several sources of mRNAs to overcome this potential problem; alternatively, this limitation can also be addressed using appropriate oligonucleotide arrays.

Iron Regulation of CDC14A mRNA—This work identifies CDC14A as a novel IRE-containing and iron-regulated mRNA. CDC14A is one of the two human orthologs of the yeast CDC14 (cell division cycle 14) gene that has been shown to encode a phosphatase involved in the dephosphorylation of several critical cell cycle proteins (37). Loss of function mutations of the *CDC14A* gene have been described in various human cancer cell lines, suggesting that CDC14A could act as a tumor suppressor (37). Indeed, CDC14A has been shown to dephosphorylate cdk substrates such as $p27^{kip1}$ and cyclin E that are critical for the G_1 to S phase progression (38). Alteration of CDC14A expression by RNA interference or transgenic overexpression has been found to cause abnormal mitotic spindle assembly and chromosome segregation (38, 39), arguing that CDC14A plays an important role in cell division.

Present and previous studies (37, 38) revealed several mRNA isoforms with heterogeneity at both the 5′- and 3′-ends of the CDC14A mRNA. These mRNA isoforms are predicted to encode different protein products that differ by their N and C termini. This heterogeneity is highly reminiscent of *SLC11A2*, another 3′-IRE-containing gene that encodes several protein isoforms (40) with distinct subcellular localizations (41, 42). Analogously, the N- and C-terminal heterogeneity of CDC14A proteins could affect the targeting of the phosphatase within the cell. Immunofluorescence studies using antibodies that do not discriminate between the CDC14A isoforms revealed both cytoplasmic and centrosomal staining (39). Here, we identify a novel 5′-exon (exon 1A) predicted to contain an *N*-myristoylation site (GNFLSR) that may target the protein to membranes (43). Further work will explore this important aspect of CDC14A biology.

The mRNA levels of the CDC14A-IRE isoforms are selectively increased upon iron deprivation of 293 and MCF7 cells. We did not observe a similar regulation in HeLa and K562 cells (data not shown). Cell type-specific iron regulation also characterizes the *SLC11A2*-IRE mRNA isoforms (44). These findings suggest that iron control of the CDC14A- and *SLC11A2*-IRE mRNA isoforms requires yet unidentified cell-specific regulatory factors, in contrast to the ubiquitous iron regulation of the *TFRC* mRNA.

What is the mechanism underlying the increase in CDC14A-IRE mRNA expression under iron-limited conditions? RT-PCR analysis demonstrated that the increase in CDC14A mRNA levels is clearly selective for the presence of the IRE in the 3′-UTR, but it does not require transcription initiation at either exon 1A or 1B. This result makes it rather unlikely that iron regulation of CDC14A mRNA expression is due to transcriptional activation, although a transcriptional mechanism cannot be ruled out formally at present. The conservation of the proposed *TFRC* mRNA endonucleolytic cleavage site in the CDC14A mRNA rather suggests the possibility that a similar mechanism of mRNA stabilization could be involved. Interestingly, the sequence conservation does not extend into the flanking sequences, which could possibly contribute to the differential regulation observed. However, CDC14A mRNA turnover was not detectably slowed in iron-deprived cells treated with DRB (supplemental Fig. S3). Although the mechanism underlying *TFRC* and CDC14 mRNA up-regulation could be distinct, it is also possible that our experimental conditions masked mRNA stabilizing effects of IRP binding. It is possible that the half-life of CDC14A mRNA significantly exceeds the time course of our DRB experiments, but this time course could not be prolonged because of the adverse toxic effects of DRB treatment. Notably, the regulation of the expression of the *SLC11A2* isoforms appears to be complex and to occur at the transcriptional, post-transcriptional, and post-translational levels (45–48). It is possible that the one or more mechanisms responsible for the iron regulation of mRNAs with single 3′-UTR IREs (*i.e.* CDC14A and *SLC11A2*) differ from the mechanism that controls the *TFRC* mRNA with 5 IRE motifs in its 3′-UTR.

Iron chelators were shown to arrest cells in the G_1/S transition by altering the expression and/or the activity of several critical cell cycle regulators (*e.g.* p53, retinoblastoma) (49, 50). Proteins important for the G_1/S transition include CDC14A substrates (*e.g.* $p27^{kip1}$ and cyclin E) (38). It is tempting to speculate that the up-regulation of CDC14A by DFO plays a role in the iron chelation-induced cell cycle arrest. The selective iron modulation of the CDC14A-IRE mRNA isoforms points toward a possible, previously unrecognized link between iron metabolism, the IRE/IRP regulatory system, and cell cycle progression.

Acknowledgments—We thank Vladimir Benes and members of the EMBL Genomics Core Facility for support with qRT-PCR and sequencing, as well as the staff of the EMBL Animal Care Facility for their dedicated support.

REFERENCES

1. Hentze, M. W., Muckenthaler, M. U., and Andrews, N. C. (2004) *Cell* **117,** 285–297
2. Eisenstein, R. S., and Ross, K. L. (2003) *J. Nutr.* **133,** 1510S–1516S
3. Schneider, B. D., and Leibold, E. A. (2000) *Curr. Opin. Clin. Nutr. Metab. Care* **3,** 267–273

4. Muckenthaler, M., Gray, N. K., and Hentze, M. W. (1998) *Mol. Cell* **2,** 383–388
5. Galy, B., Ferring, D., and Hentze, M. W. (2005) *Genesis* **43,** 181–188
6. Meyron-Holtz, E. G., Ghosh, M. C., Iwai, K., LaVaute, T., Brazzolotto, X., Berger, U. V., Land, W., Ollivierre-Wilson, H., Grinberg, A., Love, P., and Rouault, T. A. (2004) *EMBO J.* **23,** 386–395
7. Galy, B., Ferring, D., Minana, B., Bell, O., Janser, H. G., Muckenthaler, M., Schumann, K., and Hentze, M. W. (2005) *Blood* **106,** 2580–2589
8. LaVaute, T., Smith, S., Cooperman, S., Iwai, K., Land, W., Meyron-Holtz, E., Drake, S. K., Miller, G., Abu-Asab, M., Tsokos, M., Switzer, R., 3rd, Grinberg, A., Love, P., Tresser, N., and Rouault, T. A. (2001) *Nat. Genet.* **27,** 209–214
9. Smith, S. R., Ghosh, M. C., Ollivierre-Wilson, H., Hang Tong, W., and Rouault, T. A. (2006) *Blood Cells Mol. Dis.* **36,** 283–287
10. Beaumont, C., Leneuve, P., Devaux, I., Scoazec, J. Y., Berthier, M., Loiseau, M. N., Grandchamp, B., and Bonneau, D. (1995) *Nat. Genet.* **11,** 444–446
11. Kato, J., Fujikawa, K., Kanda, M., Fukuda, N., Sasaki, K., Takayama, T., Kobune, M., Takada, K., Takimoto, R., Hamada, H., Ikeda, T., and Niitsu, Y. (2001) *Am. J. Hum. Genet.* **69,** 191–197
12. Hentze, M. W., Caughman, S. W., Casey, J. L., Koeller, D. M., Rouault, T. A., Harford, J. B., and Klausner, R. D. (1988) *Gene* (*Amst.*) **72,** 201–208
13. Theil, E. C., and Eisenstein, R. S. (2000) *J. Biol. Chem.* **275,** 40659–40662
14. Bengert, P., and Dandekar, T. (2003) *Nucleic Acids Res.* **31,** 3441–3445
15. Dandekar, T., Stripecke, R., Gray, N. K., Goossen, B., Constable, A., Johansson, H. E., and Hentze, M. W. (1991) *EMBO J.* **10,** 1903–1909
16. Gray, N. K., Pantopoulos, K., Dandekar, T., Ackrell, B. A., and Hentze, M. W. (1996) *Proc. Natl. Acad. Sci. U. S. A.* **93,** 4925–4930
17. Henderson, B. R., Menotti, E., Bonnard, C., and Kuhn, L. C. (1994) *J. Biol. Chem.* **269,** 17481–17489
18. Butt, J., Kim, H. Y., Basilion, J. P., Cohen, S., Iwai, K., Philpott, C. C., Altschul, S., Klausner, R. D., and Rouault, T. A. (1996) *Proc. Natl. Acad. Sci. U. S. A.* **93,** 4345–4349
19. Meehan, H. A., and Connell, G. J. (2001) *J. Biol. Chem.* **276,** 14791–14796
20. Muckenthaler, M., Richter, A., Gunkel, N., Riedel, D., Polycarpou-Schwarz, M., Hentze, S., Falkenhahn, M., Stremmel, W., Ansorge, W., and Hentze, M. W. (2003) *Blood* **101,** 3690–3698
21. Gray, N. K., Quick, S., Goossen, B., Constable, A., Hirling, H., Kuhn, L. C., and Hentze, M. W. (1993) *Eur. J. Biochem.* **218,** 657–667
22. Church, G. M., and Gilbert, W. (1984) *Proc. Natl. Acad. Sci. U. S. A.* **81,** 1991–1995
23. Mignone, F., Grillo, G., Licciulli, F., Iacono, M., Liuni, S., Kersey, P. J., Duarte, J., Saccone, C., and Pesole, G. (2005) *Nucleic Acids Res.* **33,** D141–D146
24. Muckenthaler, M., Roy, C. N., Custodio, A. O., Minana, B., deGraaf, J., Montross, L. K., Andrews, N. C., and Hentze, M. W. (2003) *Nat. Genet.* **34,** 102–107
25. Pfaffl, M. W. (2001) *Nucleic Acids Res.* **29,** e45
26. Pantopoulos, K., and Hentze, M. W. (1995) *Proc. Natl. Acad. Sci. U. S. A.* **92,** 1267–1271
27. Goossen, B., and Hentze, M. W. (1992) *Mol. Cell. Biol.* **12,** 1959–1966
28. Lymboussaki, A., Pignatti, E., Montosi, G., Garuti, C., Haile, D. J., and Pietrangelo, A. (2003) *J. Hepatol.* **39,** 710–715
29. Benes, V., and Muckenthaler, M. (2003) *Trends Biochem. Sci.* **28,** 244–249
30. Tchernitchko, D., Bourgeois, M., Martin, M. E., and Beaumont, C. (2002) *Biochem. J.* **363,** 449–455
31. Binder, R., Horowitz, J. A., Basilion, J. P., Koeller, D. M., Klausner, R. D., and Harford, J. B. (1994) *EMBO J.* **13,** 1969–1980
32. Koeller, D. M., Casey, J. L., Hentze, M. W., Gerhardt, E. M., Chan, L. N., Klausner, R. D., and Harford, J. B. (1989) *Proc. Natl. Acad. Sci. U. S. A.* **86,** 3574–3578
33. Casey, J. L., Koeller, D. M., Ramin, V. C., Klausner, R. D., and Harford, J. B. (1989) *EMBO J.* **8,** 3693–3699
34. Mullner, E. W., Neupert, B., and Kuhn, L. C. (1989) *Cell* **58,** 373–382
35. Kohler, S. A., Menotti, E., and Kuhn, L. C. (1999) *J. Biol. Chem.* **274,** 2401–2407
36. Cmejla, R., Petrak, J., and Cmejlova, J. (2006) *Biochem. Biophys. Res. Commun.* **341,** 158–166
37. Wong, A. K., Chen, Y., Lian, L., Ha, P. C., Petersen, K., Laity, K., Carillo, A., Emerson, M., Heichman, K., Gupte, J., Tavtigian, S. V., and Teng, D. H. (1999) *Genomics* **59,** 248–251
38. Kaiser, B. K., Zimmerman, Z. A., Charbonneau, H., and Jackson, P. K. (2002) *Mol. Biol. Cell* **13,** 2289–2300
39. Mailand, N., Lukas, C., Kaiser, B. K., Jackson, P. K., Bartek, J., and Lukas, J. (2002) *Nat. Cell Biol.* **4,** 317–322
40. Hubert, N., and Hentze, M. W. (2002) *Proc. Natl. Acad. Sci. U. S. A.* **99,** 12345–12350
41. Lam-Yuk-Tseung, S., and Gros, P. (2006) *Biochemistry* **45,** 2294–2301
42. Tabuchi, M., Tanaka, N., Nishida-Kitayama, J., Ohno, H., and Kishi, F. (2002) *Mol. Biol. Cell* **13,** 4371–4387
43. Farazi, T. A., Waksman, G., and Gordon, J. I. (2001) *J. Biol. Chem.* **276,** 39501–39504
44. Gunshin, H., Allerson, C. R., Polycarpou-Schwarz, M., Rofts, A., Rogers, J. T., Kishi, F., Hentze, M. W., Rouault, T. A., Andrews, N. C., and Hediger, M. A. (2001) *FEBS Lett.* **509,** 309–316
45. Zoller, H., Theurl, I., Koch, R., Kaser, A., and Weiss, G. (2002) *Blood Cells Mol. Dis.* **29,** 488–497
46. Paradkar, P. N., and Roth, J. A. (2006) *Biochem. J.* **394,** 173–183
47. Lis, A., Paradkar, P. N., Singleton, S., Kuo, H. C., Garrick, M. D., and Roth, J. A. (2005) *Biochem. Pharmacol.* **69,** 1647–1655
48. Wang, X., Garrick, M. D., Yang, F., Dailey, L. A., Piantadosi, C. A., and Ghio, A. J. (2005) *Am. J. Physiol.* **289,** L24–L33
49. Liang, S. X., and Richardson, D. R. (2003) *Carcinogenesis* **24,** 1601–1614
50. Le, N. T., and Richardson, D. R. (2002) *Biochim. Biophys. Acta* **1603,** 31–46